DISPERSION-DISSIPATION ANALYSIS FOR ADVECTION PROBLEMS WITH NON-CONSTANT COEFFICIENTS: APPLICATIONS TO DISCONTINUOUS GALERKIN FORMULATIONS*

JUAN MANZANERO[§†], GONZALO RUBIO[†], ESTEBAN FERRER[†], AND EUSEBIO VALERO[†]

Abstract. This paper presents an extended version of von Neumann stability analysis to study dispersion and dissipation errors in non-constant coefficient advection equations. This approach is used to analyse the behaviour of discontinuous Galerkin (DG) discretisations, including the influence of polynomial order, number of elements, and choice of quadrature points (Gauss or Gauss-Lobatto) on numerical errors. Additionally, the split flux formulation (conservative, non-conservative, and skew-symmetric) and inter-element numerical fluxes (upwind or central) for non-constant coefficient problems are also studied. Our analysis demonstrates that schemes that appear stable when analysed using the classic (constant speed) von Neumann technique may reveal instabilities in cases with non-constant advection speeds (e.g., DG with Gauss-Lobatto points and central fluxes). Additionally, our analysis shows that other schemes (non-conservative DG with central fluxes and Gauss-Lobatto nodes) are stable for both constant and non-constant advection speeds.

Key words. discontinuous Galerkin, von Neumann analysis, dispersion-dissipation analysis, split formulations

AMS subject classifications. 65N12, 65N30, 65N35

1. Introduction.

The study of dispersion and dissipation properties is of interest to all numerical techniques that solve partial differential equations, including finite difference methods (FD) [20, 4], finite volume methods (FV) [45, 38], finite elements (FE) [50, 10], and high-order continuous and discontinuous spectral/hp methods [30, 26, 3, 33, 27]. These errors are typically obtained through analysis of advection-diffusion equations or non-linear equations after linearization based on a suitable equilibrium state. Von Neumann analysis estimates the dispersion and dissipation errors present in numerical discretisations by tracking the evolution of wavelike initial conditions introduced in the numerical schemes. Numerically modified amplitudes and frequencies provide information on numerical errors, thereby characterising their underlying properties. Dispersion errors represent inaccuracies in advection speed, whereas dissipation errors correspond to unphysical damping (or amplification) of the solution. Both types of errors must be analysed to appraise the accuracy of a numerical solution, but the latter is particularly crucial to understanding the stability and robustness of a numerical scheme.

Well-known examples include the selection of an approximation order for the derivatives in FD schemes [4] or the choice of numerical fluxes in FV [11] and discontinuous Galerkin methods. Certain configurations comprising a particular numerical scheme and discretisation order may present large dispersion or dissipation errors, or even lead to unstable methods. Consequently, controlling these errors is mandatory when designing new stable numerical schemes.

In recent years, high-order continuous and discontinuous Galerkin (DG) spectral/hp methods have experienced increasing popularity. These high-order methods offer favourable error properties and allow for mesh and polynomial adaption, referred

*Submitted to the editors DATE.

[†]ETSIAE-UPM - School of Aeronautics, Plaza Cardenal Cisneros 3, E-28040 Madrid, Spain

[§]Corresponding author (juan.manzanero@upm.es)

to as h-refinement and p-refinement, respectively. DG methods require the approximation of inter-element numerical fluxes (e.g., the Riemann problem for hyperbolic conservation laws) to couple discontinuous elements, thereby inheriting properties from finite volume methods. Additionally, the variational formulations in which high order techniques are set may introduce accuracy and stability issues related to the quadrature rules used to numerically evaluate integrals. Finally, advective fluxes may be discretised in various split forms (i.e., conservative, non-conservative, and skew-symmetric), which leads to differences in error behaviours and accuracy. Overall, DG schemes are flexible, adaptable and provide a broad framework for the study of physical problems.

Various researchers have worked to quantify the numerical dispersion and dissipation properties of high-order schemes in an attempt to understand their limitations and applicability when solving complex problems, such as the Navier-Stokes equations. Pioneering work includes that by Sherwin [43], who demonstrated that discontinuous Galerkin formulations were more dissipative than their continuous counterparts. Ainsworth [1] calculated the super-exponential decay rate of dispersion and dissipation for large polynomials. Hesthaven and Warburton [27] analysed the interplay between polynomial order and numerical fluxes. Gassner [18], as well as Gassner and Kopriva [22], studied the effects of polynomial order and selection of nodal points (and associated quadrature rules) on dispersion-dissipation errors, particularly for Legendre-Gauss and Legendre-Gauss-Lobatto nodes. More recently, Moura *et al.* [36] studied the complete eigensolution spectra that arises from the stability analysis of discontinuous Galerkin schemes with an emphasis on numerical secondary modes. Very recent work [46, 48] has explored nodal discontinuous Galerkin schemes from a flux reconstruction perspective for linear advection-dissipation equations and examined the associated spatio-temporal stability. All of these studies have used von Neumann analysis with constant advection speeds.

Our study generalises classic (constant advection speed) von Neumann analysis for non-constant advection speeds. It is worth mentioning that other methods do exist for analysing advection equations with non-constant speeds (e.g., technique of frozen coefficients [47]). However, we have found that the technique presented herein is better suited to the analysis of high-order methods, as well as several stabilising techniques, such as split formulations for fluxes (see [6, 7, 19, 23]). To the best of our knowledge, the approach presented herein has not been attempted in the past. In the following sections, we will demonstrate that our novel analysis technique generalises the classic technique and provides new insights into the stability of various schemes. Finally, it should be noted that non-constant advection cases may be interpreted as local accelerations of a uniform mesh or as a constant-speed on non-homogeneous distribution of mesh points (e.g., curvilinear meshes [23]).

To summarise, this work uses DG methods to explore the developed von Neumann analysis technique for non-constant advection speeds. We study DG variants that combine different polynomial orders, quadrature rules, numerical fluxes, and split formulations. We demonstrate that methods that may seem robust when considering constant speeds (e.g., DG with Gauss-Lobatto points and central fluxes) may become unstable when non-constant advection speeds are considered (see results section). We also demonstrate that other combinations (e.g., non-conservative DG with central fluxes) remain stable when considering the proposed analysis technique.

The remainder of this paper is organised as follows. In section 2, the novel dispersion-dissipation analysis technique for non-constant coefficient problems is derived. Additionally, the details of the selected DG framework are discussed in this

section. Next, section 3 explores the dispersion and dissipation behaviours of various parameters and configurations, including the effects of polynomial order, selection of nodal points, and formulation of advective fluxes (split form). Finally, in section 4, the results of our novel von Neumann analysis technique are validated through numerical experiments.

2. Methodology. First, in section 2.1, we will describe the advection equation with non-constant advection speeds and provide insights into the different split formulations for the fluxes. In section 2.2, we describe the DG implementation of the introduced formulations and compare its features to those of the constant advection speed case. Finally, in section 2.3, the methodology for performing dispersion-dissipation analysis with non-constant advection speeds is derived.

2.1. Advection differential equation. We consider a one-dimensional advection differential equation with a non-constant advection speed $a(x)$:

$$q_t + a(x)q_x = 0, \quad -L < x < L. \tag{1}$$

To analyse this problem, we adopt the generalised split formulation introduced by Gassner [17], Kopriva *et al.* [7], and Gassner *et al.* [23]:

$$q_t + \alpha f_x + (1-\alpha)[aq_x + a_x q] = a_x q, \quad -L < x < L, \tag{2}$$

where q is the transported unknown, $a(x)$ is the spatially varying advection velocity, and $f = aq$ is the flux, such that $f_x = (aq)_x = a_x q + aq_x$. The subindexes t and x denote the time and spatial derivatives, respectively. By setting $\alpha \in \mathbb{R}$ appropriately in Eq. (2), we recover the familiar forms:

- $\alpha = 1 \quad \longrightarrow$ Conservative form: $\quad q_t + (aq)_x = a_x q.$
- $\alpha = 1/2 \quad \longrightarrow$ Skew-symmetric form: $\quad q_t + \frac{1}{2}\left[(aq)_x + a_x q + aq_x\right] = a_x q.$
- $\alpha = 0 \quad \longrightarrow$ Non-conservative form: $\quad q_t + aq_x = 0.$

Note that all split forms are equivalent when the continuous version of the partial differential equation (PDE) is considered, but this is not necessarily true in the discrete version because of aliasing errors. It is convenient to introduce a periodic and continuous function $g(x)$ such that the advection speed can be written as $a(x) = \bar{a}/g(x)$. Note that the constant advection speed case can be recovered by setting $g(x) = 1$. Thus, Eq. (1) can be integrated by means of separation of variables, which yields the general expression:

$$q_t = -a(x)q_x \rightarrow \frac{dx}{dt} = \frac{\bar{a}}{g(x)} \rightarrow \int_0^x g(\xi)d\xi - \bar{a}t = G(x) - \bar{a}t = \text{const}, \tag{3}$$

where $G(x)$ denotes the primitive function of $g(x)$. Note that the general solution of the advection equation is any function of the form $q = \varphi[G(x) - \bar{a}t]$ and, in particular, a harmonic wave $q = \exp[i(G(x) - \bar{a}t)]$. The function $g(x)$ that controls advection speed $a(x)$ is restricted to be periodic in the considered domain (i.e., $g(x+2L) = g(x)$). As a result, its primitive (i.e., $G(x)$) is also periodic if the average $\bar{g}$ of $g(x)$ in the domain is zero. Using this definition, the following decomposition for $G(x)$ can be introduced:

$$G(x) = \bar{g}x + \hat{g}(x), \quad \bar{g} = \frac{1}{2L}\int_{-L}^{L} g(\xi)d\xi, \tag{4}$$

with the perturbation function $\hat{g}(x)$, which is defined as:

$$\hat{g}(x) = \int_0^x \big[g(\xi) - \bar{g}\big] d\xi. \tag{5}$$

Thus, we recover a periodical function $\hat{g}(x) = \hat{g}(x + 2L)$. From this perspective, we can distinguish two cases:

- For constant advection speeds where $\hat{g}(x) = 0$, we obtain harmonic wave eigenfunctions in their typical form:

  $$q(x,t) = \exp[i(kx - \omega t)], \tag{6}$$

  where a specific wavenumber k and frequency $\omega = \bar{a}k$ are considered. The initial condition must be consistent with Eq. (6), specifically:

  $$q_0(x) = q(x,0) = \exp[ikx]. \tag{7}$$

- For non-constant advection speeds, the eigenfunctions are extended according to Eq. (3):

  $$q(x,t) = \exp[i(\hat{k}G(x) - \omega t)], \quad q_0(x) = \exp[i\hat{k}G(x)]. \tag{8}$$

A scaled wavenumber $\hat{k}$ is defined to compare results between the constant and non-constant advection speed problems. This scaling is performed by means of the average $\bar{g}$, specifically:

$$\hat{k} = \frac{k}{\bar{g}}, \quad \omega = \bar{a}\hat{k} = \frac{\bar{a}k}{\bar{g}}. \tag{9}$$

Consequently, the frequency ω is also affected by this scaling. Substituting Eq. (9) into Eq. (8):

$$q(x,t) = \exp[i(kx + k\hat{g}(x)/\bar{g} - \bar{a}kt/\bar{g})]. \tag{10}$$

The generalised eigenfunctions for non-constant advection speeds shown in Eq. (8) are studied in our dispersion-dissipation analysis. Similar to the constant advection speed case, the eigenfunctions in Eq. (10) define a Fourier basis, meaning any periodic function can be expanded using these modes to generalize the result to more complex periodic functions.

2.2. Nodal discontinuous Galerkin spectral element method. DG methods were initially developed to solve hyperbolic equations written as conservation laws (see [28]), specifically:

$$q_t + \nabla \cdot F(q) = 0. \tag{11}$$

Subsequently, these methods were extended to elliptic equations in [12, 8], making them suitable to solve a variety of problems ranging from electromagnetics to compressible problems (e.g. [2, 21, 9, 31, 32]), incompressible problems [37, 5, 42, 14, 15, 13], and multiphase fluid dynamic problems [16, 35].

This approach divides the domain $x \in [-L, L]$ into K non-overlapping subdomains Ω^{el}. In each subdomain or element, both the solution and fluxes are approximated by polynomials of order N to obtain piecewise solutions. In this one-dimensional approach, each element $x \in [x^{el-1}, x^{el}]$ is mapped into a local domain $\xi \in [-1, 1]$ (typically referred to as a reference domain) by means of linear mapping $X^{el}(\xi)$:

$$X^{el}(\xi) = \frac{1}{2}\big(x^{el-1}(1-\xi) + x^{el}(1+\xi)\big), \quad X^{el}_{\xi} = \frac{x^{el} - x^{el-1}}{2} = \frac{h}{2}, \tag{12}$$

where x^{el-1} and x^{el} refer to the left and right boundaries of the considered element, respectively, and h denotes its length. The spectral element method approximates both the solution q and fluxes f (e.g., for the advection equation, approximating $f = a(x)q$) inside each element using polynomials of order N):

$$I^N[q(X^{el}(\xi), t)] = Q^{el}(\xi) = \sum_{j=0}^{N} Q^{el}_j l_j(\xi), \tag{13}$$

$$I^N[f(Q^{el})] = F^{el}(\xi) = \sum_{j=0}^{N} F^{el}_j l_j(\xi) = \sum_{j=0}^{N} a(X^{el}(\xi_j)) Q^{el}_j l_j(\xi) = \sum_{j=0}^{N} A^{el}_j Q^{el}_j l_j(\xi), \tag{14}$$

where I^N is a Lagrange interpolation operator based on $N+1$ interpolation nodes in the reference element $\{\xi_j\}_{j=0}^{N}$ and $l_j(\xi)$ denotes the Lagrange polynomials. These nodes are mapped using $X^{el}(\xi)$ to obtain interpolation nodes in the physical domain $\{x_j\}_{j=0}^{N}$. In this work, both Legendre-Gauss and Legendre-Gauss-Lobatto (including end-points) nodes are used as interpolation nodes. Additionally, $A^{el}(\xi) = I^N[a(x)]$ represents the discrete version of $a(x)$ and Q^k_j are the solution coefficients of each node (i.e., a nodal DG approach).

The DG method seeks solutions in the weak form. Therefore, we restrict the residuals of the discrete advection equation (split form) shown in Eq. (2) to be orthogonal to the solution space, which is spanned by the Lagrange polynomials (i.e., Galerkin approach):

$$\int_{-1}^{1} l_j \left\{ \frac{h}{2} Q^{el}_t + \alpha F^{el}_{\xi} + (1-\alpha)[A^{el} Q^{el}_{\xi} + A^{el}_{\xi} Q^{el}] \right\} d\xi = \int_{-1}^{1} l_j A^{el}_{\xi} Q^{el} d\xi, \tag{15}$$

where we recall that α determines the split form. Following [6], the terms F^{el}_{ξ} and $A^{el}Q^{el}_{\xi}$ are integrated by parts. The resulting inter-element fluxes are approximated by a numerical flux F^*:

$$\begin{aligned} &\frac{h}{2}\int_{-1}^{1} l_j Q^{el}_t d\xi + F^* l_j \Big|_{-1}^{+1} - \int_{-1}^{+1} \alpha F^{el} l'_j d\xi \\ &\qquad + (1-\alpha)\left[-\int_{-1}^{1} \big(A^{el} l_j\big)' Q^{el} d\xi + \int_{-1}^{1} A^{el}_{\xi} Q^{el} l_j d\xi \right] = \int_{-1}^{1} l_j A^{el}_{\xi} Q^{el} d\xi. \end{aligned} \tag{16}$$

This numerical flux is shared by both the left and right boundaries, and depends on the two adjacent states (i.e., $F^* = F^*(Q_L, Q_R)$). Two approaches exist to tackle the numerical quadrature of the integrals that arise from the weak formulation. The most common approach utilizes a polynomial of order N to approximate the flux.

Therefore, Gauss quadratures based on interpolation nodes are sufficiently accurate to perform the integration analytically. In contrast, the over-integration approach (see [41, 39, 24, 40]) considers a consistent approximation of the integrals arising from the weak formulation. Whilst the former approach is more computationally efficient, the latter approach reduces aliasing errors. In this work, we adopt the first approach where a polynomial of order N is used to approximate the numerical flux and Gauss quadrature rules approximate the integrals in Eq. (16). The following scheme is obtained in matrix form:

$$\begin{aligned}\frac{h}{2}\boldsymbol{M}\dot{\underline{\boldsymbol{Q}}}^{el} + F^*\underline{\boldsymbol{l}}\Big|_{-1}^{1} - \alpha\boldsymbol{D}^T\boldsymbol{M}\boldsymbol{A}^{el}\underline{\boldsymbol{Q}}^{el} \\ + (1-\alpha)\left[\boldsymbol{M}\boldsymbol{B}^{el}\underline{\boldsymbol{Q}}^{el} - \boldsymbol{A}^{el}\boldsymbol{D}^T\boldsymbol{M}\underline{\boldsymbol{Q}}^{el}\right] = \boldsymbol{M}\boldsymbol{B}^{el}\underline{\boldsymbol{Q}}^{el}.\end{aligned} \tag{17}$$

It should be noted that $\boldsymbol{M}$, $\boldsymbol{A}$, and $\boldsymbol{B}$ are diagonal matrices. Their entries are $[M_{ij}] = w_i\delta_{ij}$, $[A_{ij}] = A_i^{el}\delta_{ij}$, with δ_{ij} being the Kronecker delta and w_i being the Gauss quadrature weights (see [3]). Additionally, the Lagrange derivative matrix contains the entries $[D_{ij}] = l_j'(\xi_i)$ and $\boldsymbol{B}^{el} = \mathrm{diag}[\boldsymbol{D}\underline{\boldsymbol{A}}^{el}]$. Finally, the column vectors for the element unknowns and discrete boundary values for the Lagrange polynomials are $[Q_j] = Q_j^{el}$ and $[l_j] = l_j(\xi)$, respectively. The numerical flux, which enforces the coupling between elements, is defined as:

$$F^*(Q_L, Q_R) = a\{\{Q\}\}_{LR} - \frac{1}{2}\lambda|a|[[Q]]_{LR} = \frac{a+\lambda|a|}{2}Q_L + \frac{a-\lambda|a|}{2}Q_R, \tag{18}$$

where $\{\{Q\}\}_{nm} = (Q_n + Q_m)/2$ denotes to the arithmetic mean and $[\![Q]\!]_{nm} = Q_m - Q_n$ refers to the jumps. The numerical boundary flux is controlled by the parameter $\lambda \in \mathbb{R}$ ($\lambda = 1$ for upwind and $\lambda = 0$ for central). Precisely, for the $el-$element:

$$\begin{aligned}F^*(n) =& \frac{a^{el-1+(n+1)/2} + \lambda|a^{el-1+(n+1)/2}|}{2}\underline{\boldsymbol{l}}^T(1)\underline{\boldsymbol{Q}}^{el-1+(n+1)/2} \\ &+ \frac{a^{el+(n+1)/2} - \lambda|a^{el+(n+1)/2}|}{2}\underline{\boldsymbol{l}}^T(-1)\underline{\boldsymbol{Q}}^{el+(n+1)/2},\end{aligned} \tag{19}$$

where $n = -1$ for the left boundary and $n = 1$ for the right boundary. Additionally, a^{el-1} refers to the advection speed computed at the element left boundary $a(X^{el}(-1))$ and a^{el} refers to that computed at the right boundary $a(X^{el}(1))$. Therefore, we can rewrite Eq. (17) in compact matrix form:

$$\frac{h}{2}\dot{\underline{\boldsymbol{Q}}}^{el} = \boldsymbol{L}^{el}\underline{\boldsymbol{Q}}^{el-1} + \boldsymbol{C}^{el}\underline{\boldsymbol{Q}}^{el} + \boldsymbol{R}^{el}\underline{\boldsymbol{Q}}^{el+1}, \tag{20}$$

with

$$\begin{aligned}\boldsymbol{L}^{el} &= \frac{a^{el-1} + \lambda|a^{el-1}|}{2}\boldsymbol{M}^{-1}\underline{\boldsymbol{l}}(-1)\underline{\boldsymbol{l}}^T(1), \\ \boldsymbol{C}^{el} &= \frac{a^{el-1} + \lambda|a^{el-1}|}{2}\boldsymbol{M}^{-1}\underline{\boldsymbol{l}}(1)\underline{\boldsymbol{l}}^T(1) - \frac{a^{el} + \lambda|a^{el}|}{2}\boldsymbol{M}^{-1}\underline{\boldsymbol{l}}(-1)\underline{\boldsymbol{l}}^T(-1) \\ &\quad + \alpha\boldsymbol{M}^{-1}\boldsymbol{D}^T\boldsymbol{M}\boldsymbol{A}^{el} + \alpha\boldsymbol{B}^{el} + (1-\alpha)\boldsymbol{A}^{el}\boldsymbol{M}^{-1}\boldsymbol{D}^T\boldsymbol{M}, \\ \boldsymbol{R}^{el} &= -\frac{a^{el} + \lambda|a^{el}|}{2}\boldsymbol{M}^{-1}\underline{\boldsymbol{l}}(1)\underline{\boldsymbol{l}}^T(-1).\end{aligned} \tag{21}$$

***Remark**: The particular case for constant advection speeds $a = \bar{a}$ (equivalently $g(x) = 1$) can be recovered by setting $A^{el} = \bar{a}\boldsymbol{I}$ (with $\boldsymbol{I}$ being the identity matrix) in the expression for $\boldsymbol{C}^{el}$ in Eq. (21) such that:*

$$\alpha\bar{a}\boldsymbol{M}^{-1}\boldsymbol{D}^T\boldsymbol{M} + \alpha\cancelto{0}{\boldsymbol{B}^{el}} + (1-\alpha)\bar{a}\boldsymbol{M}^{-1}\boldsymbol{D}^T\boldsymbol{M} = \bar{a}\boldsymbol{M}^{-1}\boldsymbol{D}^T\boldsymbol{M}. \tag{22}$$

Note that in the constant speed case, the algorithm does not depend on α, meaning it is independent of the flux form: conservative, skew-symmetric, or non-conservative.

To account for multiple elements (with equispaced vertices), we consider the direct sum of K-element contributions, as shown in Eq. (20). The resulting column vector of total unknowns $\underline{\boldsymbol{Q}}$ is constructed by combining all element degrees of freedom $\underline{\boldsymbol{Q}} = [\underline{\boldsymbol{Q}}^1, \underline{\boldsymbol{Q}}^2, ..., \underline{\boldsymbol{Q}}^K]^T$. The effect of the physical boundary conditions is introduced through two ghost elements, $\underline{\boldsymbol{Q}}^0$ and $\underline{\boldsymbol{Q}}^{K+1}$, which are added to represent external states. These can be regarded as the continuation of a hypothetical infinite mesh because von Neumann analysis is formulated in an infinite domain (see section 2.3). The resulting complete discrete system for K elements is defined as:

$$\frac{h}{2}\dot{\underline{\boldsymbol{Q}}} = \boldsymbol{C}\cdot\underline{\boldsymbol{Q}} + \boldsymbol{L}\cdot\underline{\boldsymbol{Q}}^0 + \boldsymbol{R}\cdot\underline{\boldsymbol{Q}}^{K+1}, \qquad \underline{\boldsymbol{Q}} = [\underline{\boldsymbol{Q}}^1, \underline{\boldsymbol{Q}}^2, ..., \underline{\boldsymbol{Q}}^K]^T, \tag{23}$$

where the matrices $\boldsymbol{C}$, $\boldsymbol{L}$, and $\boldsymbol{R}$ are block matrices built using the element-wise DG matrices $\boldsymbol{L}^{el}$, $\boldsymbol{C}^{el}$, and $\boldsymbol{R}^{el}$. The matrices for the complete system are detailed in Appendix A. The final two terms in Eq. (23) act as source terms and account for periodic boundary conditions.

2.3. Dispersion-dissipation analysis for non-constant advection speeds. The Von Neumann or dispersion-dissipation analysis compares the analytical solution of an advection equation to the numerical solution. Here, we present a novel method that extends the classical analysis technique to non-constant advection speed problems. Additionally, this method is used to study various DG configurations and reveal numerical behaviours that only emerge when considering non-constant speeds. The non-constant speed problem is relevant because it describes accelerations in uniform meshes or, alternatively, the effect of metric terms arising from non-uniform element distributions when solving the constant speed problem (e.g., curvilinear meshes). Our analysis encompasses these problems in a unique framework and generalises the well-known von Neumann analysis technique to more complex problems.

Spatial discretisation of the advection equation is performed by means of the discontinuous Galerkin method described in section 2.2, whereas temporal evolution is analytical, meaning only spatial errors are considered. Our method analyses the wave-like eigenfunctions of the non-constant speed advection equation, as shown in Eq. (1). The domain $x \in [-L, L]$ is tessellated using K elements. The initial condition for a given wavenumber is obtained directly from Eq. (8):

$$Q_j^{el}(0) = \exp[i(\hat{k}G(x_j^{el}))]. \tag{24}$$

The ODE system summarised in Eq. (23) describes the time evolution of all degrees of freedom $Q_j^k(t)$ and includes ghost cells to account for periodic boundary conditions. For periodic advection speeds (i.e., $a(x) = a(x + 2L)$), we can expand $G(x)$ using its

average $\bar{g}$ and a perturbation $\hat{g}$ by following Eq. (4) to obtain the initial condition for the left ghost cell:

$$Q_j^0(0) = \exp[i(kx_j^0 + \hat{k}\hat{g}(x_j^0))] = \exp[i(kx_j^K - 2kL + \hat{k}\hat{g}(x_j^K))] \\ = \exp[-2ikL]Q_j^K(0), \tag{25}$$

which is linked to the final element. Similarly, for the right ghost cell, we obtain:

$$Q_j^{K+1}(0) = \exp[i(kx_j^{K+1} + \hat{k}\hat{g}(x_j^{K+1}))] = \exp[i(kx_j^1 + 2kL + \hat{k}\hat{g}(x_j^1))] \\ = \exp[2ikL]Q_j^1(0), \tag{26}$$

which is linked to the first element. Eqs. (25) and (26) are replaced in Eq. (23) to alter the coefficient matrix $\boldsymbol{C}$, thereby modifying the system as:

$$\frac{h}{2}\dot{\underline{\boldsymbol{Q}}} = \boldsymbol{C}\cdot\underline{\boldsymbol{Q}} + \exp[-2ikL]\boldsymbol{L}\cdot\underline{\boldsymbol{Q}}^K + \exp[2ikL]\boldsymbol{R}\cdot\underline{\boldsymbol{Q}}^1 = \boldsymbol{M}(k)\cdot\underline{\boldsymbol{Q}}. \tag{27}$$

Following this condensation, we obtain a homogeneous system of linear ordinary differential equations, whose solution is a linear combination of modes:

$$\underline{\boldsymbol{Q}}(t) = \sum_{m=1}^{(N+1)K} A_m\underline{\boldsymbol{v}}_m\exp[-i\omega_m t], \quad \lambda_m = -i\omega_m\frac{h}{2}, \quad \lambda_m\underline{\boldsymbol{v}}_m = \boldsymbol{M}(k)\underline{\boldsymbol{v}}_m, \tag{28}$$

where λ_m and $\underline{\boldsymbol{v}}_m$ are the eigenvalues and eigenvectors of the coefficient matrix $\boldsymbol{M}(k)$, respectively, while A_m are constants obtained from the projection of the initial condition onto the space spanned by the eigenvectors. Eq. (28) can be regarded as a superposition of waves that travel according to their advection speed ω_m. Therefore, we define the numerical wave travelling speed $k^\star$ as:

$$k^\star = \frac{\bar{g}\,\mathrm{Re}(\omega)}{\bar{a}}, \tag{29}$$

and the numerical dimensionless dissipation γ as:

$$\gamma = -\frac{\bar{g}\,\mathrm{Im}(\omega)}{\bar{a}k}. \tag{30}$$

Recall that the analytical solution satisfies $k^\star = k$ and $\gamma = 0$. When the solution is separated into modes, the initial condition is projected onto the eigenvector basis. Only one of the modes tracks the physical propagation speed and damping. This mode is referred to as the primary mode. All remaining modes are spurious and are referred to as secondary modes (see [36]). The primary mode can be isolated from the other modes to highlight the impact of the secondary modes in the solution:

$$\underline{\boldsymbol{Q}}^{el} = \sum_{m=0}^{N} A_m\underline{\boldsymbol{v}}_m e^{i\omega_m t} = A_p\underline{\boldsymbol{v}}_p e^{i\omega_p t} + \sum_{\substack{m=0\\ m\neq p}}^{N} A_m\underline{\boldsymbol{v}}_m e^{i\omega_m t}. \tag{31}$$

Additionally, because the solution satisfies the initial condition, the amplitudes A_m can be computed:

$$\{e^{ikx_j^{el}}\}_{j=0}^{N} = \underline{\boldsymbol{q}}_0 = \sum_{m=0}^{N} A_m \underline{\boldsymbol{v}}_m = \boldsymbol{V}\underline{\boldsymbol{A}}. \tag{32}$$

Applying a similar splitting function to that in Eq. (31), we obtain:

$$\{e^{ikx_j^{el}}\}_{j=0}^{N} = \underline{\boldsymbol{q}}_0 = \sum_{m=0}^{N} A_m \underline{\boldsymbol{v}}_m = A_p \underline{\boldsymbol{v}}_p + \sum_{\substack{m=0 \\ m\neq p}}^{N} A_m \underline{\boldsymbol{v}}_m. \tag{33}$$

By Eq. (33) in Eq. (31), we can derive an expression for the numerical errors in terms of primary and secondary modes:

$$\begin{aligned} \underline{\boldsymbol{Q}}^{el} = \sum_{m=0}^{N} A_m \underline{\boldsymbol{v}}_m e^{i\omega_m t} &= \left(\underline{\boldsymbol{q}}_0 - \sum_{\substack{m=0 \\ m\neq p}}^{N} A_m \underline{\boldsymbol{v}}_m\right) e^{i\omega_p t} + \sum_{\substack{m=0 \\ m\neq p}}^{N} A_m \underline{\boldsymbol{v}}_m e^{i\omega_m t} \\ &= \underline{\boldsymbol{q}}_0 e^{i\omega_p t} + \sum_{\substack{m=0 \\ m\neq p}}^{N} A_m \underline{\boldsymbol{v}}_m \left(e^{i\omega_m t} - e^{i\omega_p t}\right). \end{aligned} \tag{34}$$

According to Eq. (34), the primary mode carries the initial condition, whereas the secondary modes can be regarded as additional numerical errors, which include dispersive and dissipative contributions. Henceforth, we distinguish three sources of numerical errors: the primary mode dispersion error, primary mode dissipation error, and errors associated with the secondary modes $\Delta\underline{\boldsymbol{q}}_s(t)$ (including dispersion and dissipation):

$$\underline{\boldsymbol{Q}}^{el} = \underline{\boldsymbol{q}}_0 e^{i\omega_{p,r} t} e^{-\omega_{p,i} t} + \Delta\underline{\boldsymbol{q}}_s(t) = \underline{\boldsymbol{q}}_0 e^{iak^\star t} e^{-ak\gamma t} + \Delta\underline{\boldsymbol{q}}_s(t). \tag{35}$$

The numerical solution propagates faster than the physical solution if $k^\star > k$ and more slowly than the physical solution if $k^\star < k$. In a similar manner, the dissipation coefficient γ modulates the solution amplitude, which is reduced if $\gamma > 0$ and amplified otherwise. Obtaining the relationship between $k^\star(k)$ and $\gamma(k)$ is the goal of dispersion-dissipation or von Neumann analysis.

2.4. Summary of our method. A von Neumann analysis technique for non-constant advection speed equations was introduced in the previous subsections. This method has been particularised to a nodal discontinuous Galerkin spectral element method (described in section 2.2), but the proposed technique can also be applied to other spatial discretisations. In this case, using the DG formulation, we are able to study the effects of the following parameters:

- Number of elements (K). The number of equally spaced divisions of the physical domain.
- Polynomial order (N). This determines the stencil dimension in each element.
- Numerical flux behaviours (λ). The case of $\lambda = 1$ refers to the case with upwind fluxes, whereas $\lambda = 0$ indicates central fluxes.
- Interpolation and quadrature nodes $\{\xi_j\}_{j=0}^{N}$. We use Legendre-Gauss and Legendre-Gauss-Lobatto points.

- Split form coefficient (α). Specifically, we consider three split forms: the conservative form ($\alpha = 1$), skew-symmetric form ($\alpha = 1/2$), and non-conservative form ($\alpha = 0$).
- The advection speed function $a(x)$, which is defined in following sections.

In section 3, this non-constant analysis technique will be applied to two different DG settings:

1. The standard DG (i.e., the conservative form) with Gauss nodes and upwind fluxes. This option is selected because it represents the traditional DG form and is one of the most widely studied and implemented forms (e.g., [33, 36, 14]).
2. The split DG form with Gauss-Lobatto nodes and central fluxes. This option is included because it represents the current trend for addressing under-resolved turbulent problems (see [21]). Gauss-Lobatto node DG methods satisfy all formal definitions of summation-by-parts (SBP) and simultaneous-approximation-term (SAT) schemes (see [19]). Therefore, these schemes are provably stable (see [44]). To analyse this configuration, it is essential to study the non-homogeneous advection speed equation. Otherwise, all split forms will be algebraically identical (see Eq. (22)).

3. Eigenvalue analysis. This section discusses the results of von Neumann stability analysis for non-constant advection speeds. We set $a(x)$ to be dependent on a parameter ε, which controls the amplitude of the inhomogeneity in $a(x)$. We restrict our study to positive and periodic non-constant advection speeds such that $a(x) > 0 \Leftrightarrow \varepsilon \in [0, 1)$. Without loss of generality, in this work, we select the first harmonic sinusoidal function:

$$a(x) = \bar{a}[1 + \varepsilon \cos\left(\frac{\pi x}{L}\right)], \tag{36}$$

where $\bar{a}$ is the average speed. Note that higher harmonic functions could be considered, but would be equivalent to subdividing the computational domain.

From Eq. (36), the inverse advection speed $g(x)$ in Eq. (3) is obtained as:

$$g(x) = \frac{1}{1 + \varepsilon \cos\left(\frac{\pi x}{L}\right)}, \tag{37}$$

which yields the advection speed primitive function $G(x)$ after integration, as defined in Eq. (3):

$$G(x) = \int_{-L}^{x} g(\xi) d\xi = -\frac{2L\left[\tanh^{-1}\left(\frac{\tan\left(\frac{\pi}{2}\frac{x}{L}\right)+\varepsilon}{\sqrt{\varepsilon^2-1}}\right) - \tanh^{-1}\left(\frac{\tan\left(-\frac{\pi}{2}\right)+\varepsilon}{\sqrt{\varepsilon^2-1}}\right)\right]}{\pi\sqrt{\varepsilon^2-1}}. \tag{38}$$

Following Eq. (4), we compute the average $\bar{g}$ of $g(x)$ in the physical domain:

$$\bar{g} = \frac{1}{2L}\int_{-L}^{L} g(\xi) d\xi = \frac{\tanh^{-1}\left(\frac{\tan\left(-\frac{\pi}{2}\right)+\varepsilon}{\sqrt{\varepsilon^2-1}}\right) - \tanh^{-1}\left(\frac{\tan\left(\frac{\pi}{2}\right)+\varepsilon}{\sqrt{\varepsilon^2-1}}\right)}{\pi\sqrt{\varepsilon^2-1}}. \tag{39}$$

Using $G(x)$ and $\bar{g}$, we can analyse the accuracy of the DG configurations.

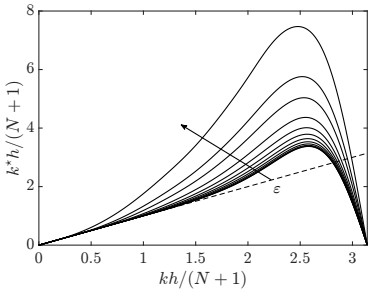

(a) Dispersion error.

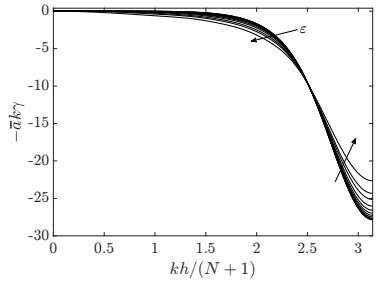

(b) Dissipation error.

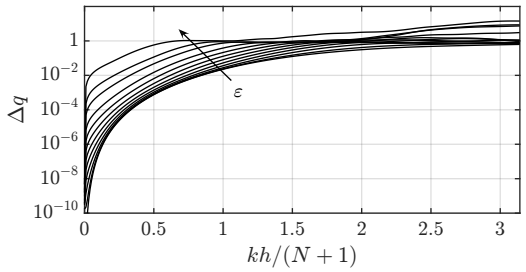

(c) Secondary mode error.

FIGURE 1. *Effects of advection speed inhomogeneity (i.e., its deviation from the constant advection speed case) on scheme accuracy, controlled by the parameter ε. It should be noted that non-constant advection speeds decrease the schemes inherent accuracy not only in terms of dispersion and dissipation, but also in terms of the errors of the secondary modes (i.e., the projection of the initial condition onto the secondary modes). Thus, to maintain a certain accuracy level, there is a need to either refine the mesh or move towards higher polynomial orders.*

3.1. Eigenvalues with Gauss points and upwind fluxes. In this section, we analyse the effect of a non-constant advection speed on schemes that have already been studied for constant speeds (see [27, 22, 36]). The standard DG uses the conservative form with Gauss points and upwind fluxes, and is analysed first. Therefore, we solve Eq. (20) with $\alpha = 1$ and $\lambda = 1$. In this test, the physical domain $x \in [-1, 1]$ is divided into $K = 4$ elements, where $N = 5$ order polynomials are used. The advection speed is that presented in Eq. (36), where we vary the parameter ε to reveal the effect of considering non-constant speed problems. We start from $\varepsilon = 0$, which represents the constant speed case, and then move towards inhomogeneous advection speeds.

In Figure 1, numerical dispersion, dissipation, and secondary mode errors are plotted against the normalised wavenumber $\bar{k} = kh/(N + 1)$. In these curves, only the primary mode is represented because when using upwind fluxes, all secondary modes are replications of the primary mode (as described in previous works [36, 34]). In the figure, the arrows represent increasing inhomogeneous speeds ε, which vary linearly from $\varepsilon = 0$ (i.e., where the constant advection speed results are recovered) to $\varepsilon = 0.6$.

Dispersion errors ($k^\star h/(N + 1)$) are shown in Figure 1(a). In this figure, the dispersion errors have been normalised by the number of degrees of freedom. The dashed

line represents the theoretical linear solution $k^* = k$. Generally speaking, if the primary mode does not follow the analytical curve, then the numerical errors are large enough to require hp-refinement. More specifically, Moura et al. [36] defined a criteria to distinguish between resolved and under-resolved simulations. They considered a simulation to be under-resolved when the relative change with respect to the theoretical linear slope in the dispersion errors was larger than 1% (i.e., $|k - k^\star| > 0.01k$) and called this criteria the 1% rule. Using this rule in our analysis, we observed that increasing advection speed inhomogeneity ε reduces the wavenumber associated with the 1% rule wavenumber $\bar{k}_{1\%}$, where $\bar{k} = kh/(N+1)$, which decreases overall scheme accuracy. Additionally, Figure 1(a) demonstrates that the dispersion error peak (beyond the 1%-rule wavenumber threshold) that arises when considering upwind fluxes increases with large inhomogeneity ε. We can conclude that the effect of considering a non-constant speed is the deterioration of the accuracy of the method, which increases the need for mesh refinement when compared to the constant speed case.
A guideline is presented in Table 1, where the 1% wavenumber has been estimated for several polynomial orders and mesh sizes. We summarise the results for $\varepsilon = 0$ (i.e., constant advection where $\bar{k}^0_{1\%}$) and $\varepsilon = 0.4$ where $\bar{k}^{0.4}_{1\%}$. Additionally, we include a more traditional estimate [27] $\bar{k}^0_{1\%}/\max(a)$ by scaling the wavenumber based on the maximum value of the advection speed instead of its average $\bar{a}$. When comparing these estimates to our more precise results, we observed that the estimated values resulted in a more conservative criteria such that for all cases $\bar{k}^{0.4}_{1\%} > \bar{k}^0_{1\%}/\max(a)$. Additionally, the parenthesis contain the ratios between $\bar{k}^0_{1\%}/\max(a)$ and $\bar{k}^{0.4}_{1\%}$. These ratios may be interpreted as the number of extra unnecessary mesh elements K that one would require if the traditional estimate $\bar{k}^0_{1\%}/\max(a)$ was used instead of the precise estimate provided by our analysis.

Dissipation errors ($\bar{a}k\gamma$) are presented in Figure 1(b). Because the analytical solution to the advection equation has no dissipation (i.e., $\gamma = 0$), obtaining values below the axis $\gamma = 0$ entails numerical energy dissipation. It should be noted that the effect of non-constant speeds is increased dissipation for well-resolved problems and decreased dissipation for under-resolved problems, which is typically an undesirable property.
We can conclude that advection speed inhomogeneity contributes to a decrease in scheme accuracy in terms of both dispersion and dissipation errors. As a result, non-constant speeds require additional spatial refinement when compared to well-resolved constant speed cases.

Finally, we present the errors associated with the secondary modes in Figure 1(c). Secondary mode errors are computed by projecting the initial condition onto the secondary modes, as described in Eq. (34). Therefore, in the constant speed case ($\varepsilon = 0$), we distinguish two regions. First, for low wavenumbers, there is a spectral convergence region because secondary mode errors decrease exponentially. Second, for large wavenumbers, the secondary mode errors reach the asymptotic value of 1, which means that the solution is completely dominated by secondary modes (both unphysical and spurious). In summary, increasing ε has two adverse effects. First, secondary mode errors increase, maintaining the constant speed slope (i.e., a pure translation towards higher errors). Second, the spectral convergence region is narrowed to lower wavenumbers.

This analysis reveals that solving non-constant advection speed problems has a significant impact in terms of solution accuracy and the smallest scales that can be captured (the 1% wavenumber). Therefore, it is necessary to use a refined mesh (increasing the number of mesh elements or the polynomial order) when considering

TABLE 1

Wavenumbers for the 1% dispersion error (i.e., dimensionless version $\bar{k} = kh/(N+1)$) while varying h (element size) and N (polynomial order). These values have been estimated for $\varepsilon = 0.4$. The constant case wavenumber ($\varepsilon = 0$) is shown in the sixth column $\bar{k}^0_{1\%}$ and the traditional estimation obtained by dividing the constant wavenumber by the highest value of the advection speed is shown in the final column. The parenthesis contain the ratios between $\bar{k}^0_{1\%}/\max(a)$ and $\bar{k}^{0.4}_{1\%}$, where $\max(a) = \bar{a}(1+\varepsilon) = 1 \times (1+0.4) = 1.4$.

		Non-constant with $\varepsilon = 0.4$				Constant ($\varepsilon = 0$)	
N	$\bar{k}_{1\%}$:	h=0.5	h=0.25	h=0.125	h=0.0625	$\bar{k}_{1\%}$	$\bar{k}_{1\%}/\max(a)$
2		0.88 (1.24)	0.92 (1.30)	0.92 (1.30)	0.93 (1.31)	1.00	0.71
3		1.03 (1.21)	1.06 (1.25)	1.07 (1.26)	1.09 (1.28)	1.19	0.85
4		1.17 (1.24)	1.19 (1.27)	1.20 (1.28)	1.21 (1.29)	1.32	0.94
5		1.29 (1.28)	1.29 (1.28)	1.29 (1.28)	1.29 (1.28)	1.42	1.01
6		1.37 (1.28)	1.36 (1.27)	1.36 (1.27)	1.36 (1.27)	1.49	1.07
7		1.43 (1.29)	1.42 (1.28)	1.41 (1.27)	1.41 (1.27)	1.56	1.11

non-constant speeds. Additional convergence results for hp-refinement are included in Appendix B.

3.2. Results with central fluxes and Gauss-Lobatto nodes. The constant speed problem solved using Gauss-Lobatto points and central fluxes ($\lambda = 0$) obtains zero dissipation $\gamma = 0$ for all wavenumbers. These eigenvalues were represented in Figure 4.7 in [27]. This is a well-known behaviour related to the lack of dissipation associated with central fluxes. The lack of numerical dissipation introduced by central fluxes may lead to instabilities (i.e., cases where $\gamma > 0$) because of aliasing errors incurred during approximation. The complexity behind the removal of aliasing errors has lead us to devote a complete publication to this topic [29], where we included theoretical continuous and discrete bounds (based on elliptic norms), and described how to perform effective removal of aliasing errors (e.g., zero dissipation, $\gamma = 0$, even with non-constant speeds) by choosing an appropriate split form parameter α.

In this work, we perform von Neumann analysis on different split formulations for non-constant advection speeds, which were summarised in Eq. (2). We will study the stability of the scheme and provide insights into how split formulations alter the dispersion and dissipation errors that are present in the scheme. In this section, we maintain the mesh used in the previous case with $K = 4$ elements and $N = 5$ order polynomials. Henceforth, the inhomogeneous non-constant advection speed parameter is fixed as $\varepsilon = 0.4$.

Dispersion and dissipation errors are presented in Figures 2, 3, and 4 for conservative, skew-symmetric, and non-conservative forms, respectively. In these figures, both primary and secondary modes are represented. Because the total number degrees of freedom is NDOF $= K(N+1) = 4(5+1) = 24$, 24 modes are represented.

First, dispersion errors are presented in Figures 2(a), 3(a), and 4(a). We note that the split operator does not have any effect on dispersion errors. Unlike in the upwind case, when using central fluxes, the modes divide into several groups. Although most of them (precisely 10 modes) are replications of the primary mode, similar to what was observed in the upwind case, another group of modes presents dispersion errors with higher frequencies. This feature is not a result of analysis of the non-constant speed problem, but is a result of the central fluxes, as described in [27]. It has also

been observed for continuous Galerkin discretisations [34].

Additionally, we represent the dissipation errors exhibited by the conservative ($\alpha = 1$), skew-symmetric ($\alpha = 1/2$), and non-conservative ($\alpha = 0$) DG configurations in Figures 2(b), 3(b), and 4(b) respectively. Figure 2(b) depicts the dissipation errors for the conservative split form ($\alpha = 1$). This DG configuration is unstable and yields two unstable modes (highlighted in red). Specifically, it provides a solution that grows exponentially if these modes are activated through the initial projection, as demonstrated by the numerical experiments in section 4. Because the primary mode and its replications present zero dissipation errors, instability is driven entirely by secondary modes.

Next, we will examine how split forms can reduce this instability. The dissipation for the skew-symmetric formulation ($\alpha = 1/2$) is presented in Figure 3(b). The skew-symmetric formulation reduces instability by approximately half, but the dispersion errors are not altered. Thus, the skew-symmetric formulation is useful for cases in which $a(x)$ changes its sign because it matches the original PDE strong-stability bound, as described in [25, 6] Therefore, it is provably stable. However, the analytical solution studied in our von Neumann analysis is restricted to $a(x) > 0$. Therefore, in this case, the analytical solution does not exhibit any energy growth (see [29]).

To replicate the behaviour of the original continuous PDE, we consider the non-conservative form ($\alpha = 0$). The dissipation introduced by the non-conservative DG is presented in Figure 4(b), where it is confirmed that this form leads to $\gamma = 0$. We can conclude that the secondary modes that made the scheme unstable when other formulations were used can be stabilised by using the non-conservative form. This DG configuration is desirable for solving problems in which the non-constant advection speed $a(x)$ is strictly positive.

To summarize, the stability of the numerical scheme increases as α (controlling the split formulation) approaches zero (i.e., non-conservative DG). This stabilisation recovers the result from the constant advection speed case in terms of dissipation errors (i.e., $\gamma = 0$). If the split form provides sufficient stabilisation, then it is not necessary to include additional dissipation as we did in the case of upwind fluxes.

To precisely demonstrate the effect of α on stability, the dissipation of the most unstable mode is tracked and illustrated in Figure 5. The effect of ε was also considered. Analysis reveals that there is a range for the split operator coefficient α in which an energy conserving scheme is recovered. This region depends on the inhomogeneity magnitude ε and narrows as advection speed oscillations increase. It should be noted that this stable region is always centred around $\alpha = 0$. Therefore, to ensure energy conservation for all inhomogeneities, the non-conservative form must be selected. Formal energy bounds to provide insights into split form behaviour have been derived and discussed by the authors in [29]. Finally, we note that dispersion errors are not altered by the split form.

4. Numerical experiments. To validate the dispersion and dissipation errors obtained above, we perform numerical experiments with various DG settings. In these experiments, the initial condition is an eigenfunction of the advection equation with the advection speed $a(x)$ selected, as shown in Eq. (38). The linear system described in Eq. (20) is integrated by means of a three-stage low-storage Runge-Kutta (RK3) algorithm [49]. Additionally, all simulations are performed with small enough time steps that temporal errors and temporal stability do not influence the results. Two test cases are presented: the first test validates our results regarding the effect of the split operator on stability and the second test provides insights into the effects of the

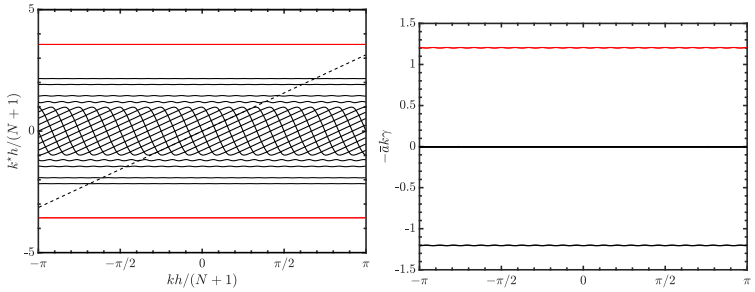

(a) Dispersion error. (b) Dissipation error.

FIGURE 2. *Conservative DG ($\alpha = 1$) dispersion-dissipation errors. The domain is divided into $K = 4$ elements with a polynomial order of $N = 5$. Central fluxes are considered ($\lambda = 0$) and polynomials are based on Gauss-Lobatto nodes. The inhomogeneity in the advection speed is fixed as $\varepsilon = 0.4$.*

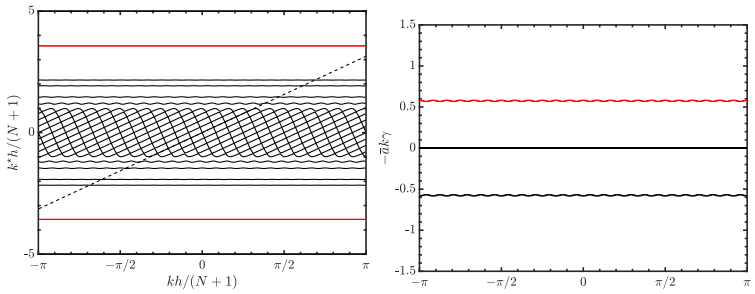

(a) Dispersion error. (b) Dissipation error.

FIGURE 3. *Skew-symmetric DG ($\alpha = 1/2$) dispersion-dissipation errors. The domain is divided into $K = 4$ elements with a polynomial order of $N = 5$. Central fluxes are considered ($\lambda = 0$) and polynomials are based on Gauss-Lobatto nodes. The inhomogeneity in the advection speed is fixed as $\varepsilon = 0.4$.*

numerical fluxes and wavenumber range characterising the initial condition.

4.1. First test: Stabilising effect of the split operator. The purpose of the first numerical experiment is to validate the results presented for the split operator parameter α. In this case, a fixed value for the wavenumber (or wavelength) is considered and the parameter ε is set to 0.12 (i.e., fixed curve for all cases shown in Figure 5). For the $\varepsilon = 0.12$ case, dissipation is controlled by the parameter α, as depicted in Figure 6(a). We performed the simulations for several α values to validate the predicted behaviour. The resulting discrete energy is depicted in Figure 6(b). The dispersion-dissipation analysis revealed a common pattern in which zero dissipation error (i.e., consistent with the analytical solution) was maintained until the α parameter reached a critical value $\alpha^\star$ (which depends on ε, in this case fixed as $\varepsilon = 0.12$ to obtain $\alpha^\star \simeq 0.5$). From this $\alpha^\star$ value, the solution becomes unstable. The slopes of the curves yield a measure of the dissipation error, which becomes larger as α increases. These results validate the effects of the split operator α that were discussed in our dispersion-dissipation analysis.

4.2. Second test: Effect of numerical fluxes and the solution wavenumber range. The dispersion-dissipation analysis for non-constant speed advection

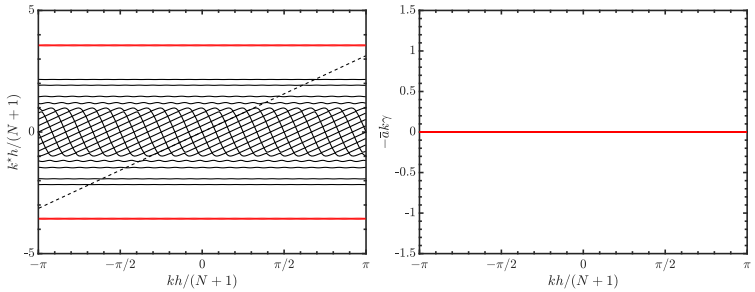

(a) Dispersion error. (b) Dissipation error.

FIGURE 4. *Non-conservative DG ($\alpha = 0$) dispersion-dissipation errors. The domain is divided into $K = 4$ elements with a polynomial order of $N = 5$. Central fluxes are considered ($\lambda = 0$) and polynomials are based on Gauss-Lobatto nodes. The inhomogeneity in the advection speed is fixed as $\varepsilon = 0.4$.*

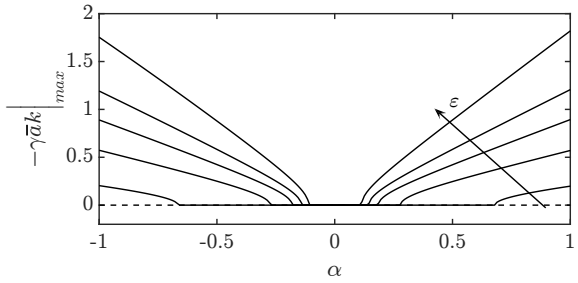

FIGURE 5. *Effect of the split operator coefficient α on the unstable mode exponent. Advection speed inhomogeneity ε varies linearly from* 0.1 *to* 0.5.

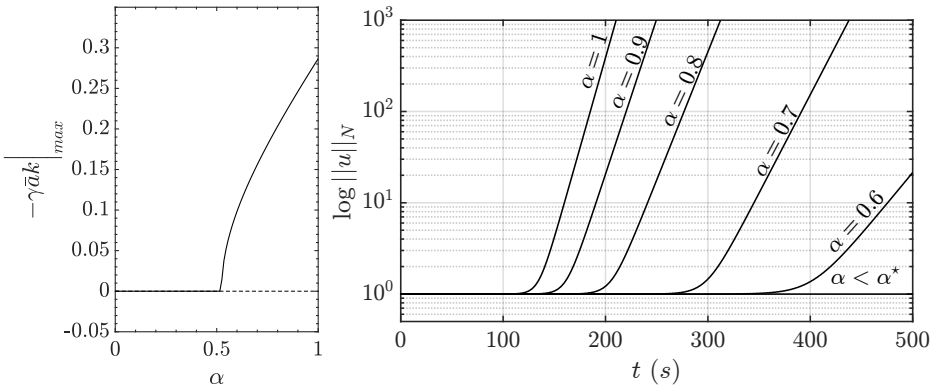

(a) Von Neumann analysis. (b) Numerical results.

FIGURE 6. *Effects of the split operator coefficient α on the stability of the solution. Figure depicts the solution energy $||u||_N$ over time. The DG discretisation considers a polynomial order of $N = 5$ with $K = 4$ elements and the advection speed parameter ε is set as* 0.12. *Numerical fluxes are central and the time step used to perform the simulations was 10^{-3} s. These results confirm the instabilities predicted by the von Neumann analysis, as well as the $\alpha^\star$ value that separates the regions where energy grows or maintains its initial value.*

equations revealed different behaviours depending on both the wavenumber analysed and the numerical flux enforced. We performed numerical experiments to prove these results. Three wavenumbers are considered: low (below $k_{1\%}$), medium (approximately $k_{1\%}$), and high (above $k_{1\%}$) wavenumbers. All cases were solved with periodic boundary conditions. Therefore, these three cases were tested with three algorithms: the standard DG method with central fluxes (A), standard DG method with upwind fluxes (B), and non-conservative formulation with central fluxes (C). A summary of the parameters for these cases is included in Table 2.

Results for the maximum value (i.e., the L^∞ norm) of the time derivative versus the number of iterations are plotted in Figure 7. In the analytical solution, the initial condition residual (i.e., the maximum derivative) remained constant over time. Furthermore, its value was assigned by the initial condition. For the upwind case, the energy was approximately preserved in the short wavenumber case because secondary modes were not predominant and we could neglect primary mode dispersion errors. Next, in the medium wavenumber case, secondary modes were either negligible compared to the primary mode or damped if activated (see [36]). In this wavenumber range, the primary mode was damped sufficiently to present a noticeable decrease in the residuals obtained. Finally, in the large wavenumber case, the high dissipation associated with the primary mode lead to decay during the first iterations. Then, the secondary modes, which are generally not damped, propagated an unphysical solution.

The conservative split form $\alpha = 1$ with Gauss-Lobatto nodes and central fluxes yielded an unstable simulation for all wavenumber ranges. This was expected based on the dispersion-dissipation analysis since Figure 2(b) showed that secondary mode instabilities are present for all wavenumbers. The main difference between the three numerical experiments was in whether this mode was more or less activated. Because all modes are always activated (although their projection onto the initial condition may be negligible compared to the rest), the solution always diverges because of the presence of unstable modes. As shown in Figure 7, in the short wavenumber range, the unstable mode was only slightly activated, meaning a large number of iterations was required to unmask the instability. The solution followed the analytical behaviour until the unstable mode amplitude became large enough to dominate the solution. Next, for the medium wavenumber case, the energy obtained was similar to the short wavenumber case because it followed the analytical solution in the first iterations (because of a small initial projection onto the unstable modes), but its growth then became noticeable and the solution diverged (after fewer iterations than in the short wavenumber case). Finally, in the high wavenumber range, the unstable mode is activated in the initial iterations, meaning the solution diverged immediately. Furthermore, the fact that the dissipation $\gamma \bar{a} k$ was approximately constant for all wavenumbers (see Figure 2(b)) resulted in a similar slope for all three cases. The only difference between the three cases was the point at which the solution diverged, which depends on the projection of the initial condition onto the unstable modes.

Finally, we consider the non-conservative ($\alpha = 0$) DG with central fluxes. The results presented in Figure 4(a) predict that the initial amplitude will be maintained in all modes (i.e., dissipation errors are negligible). The short wavenumber case activated only the primary mode and the influence of secondary modes was negligible. In this case, the analytical solution was accurately maintained during all iterations. When considering both medium and large wavenumber cases, the secondary modes were activated. Therefore, the residual plot exhibited oscillations. These oscillations can be attributed to the superposition of primary and secondary modes, which

TABLE 2

Numerical experiments summary. The parameters represented are the normalised wavenumber $kh/(N+1)$ (three cases: low, medium, and high wavenumbers), the inhomogeneity amplitude ε (fixed in this test case), the split operator parameter α ($\alpha = 0$ represents non-conservative DG and $\alpha = 1$ represents conservative DG), the numerical flux type λ ($\lambda = 0$ represents central fluxes and $\lambda = 1$ represents upwind fluxes), and the nodes distribution type $\{\xi_j\}_{j=0}^{N}$ (LG is Legendre-Gauss nodes and LGL is Legendre-Gauss-Lobatto nodes). ***Crossed case labels refer to diverging results.***

Case	$kh/(N+1)$	ε	α	λ	$\{\xi_j\}_{j=0}^{N}$
~~A1~~	$\pi/4$	0.4	1.0 (Cons)	0.0 (Central)	LGL
~~A2~~	$3\pi/4$	0.4	1.0 (Cons)	0.0 (Central)	LGL
~~A3~~	$\pi/2$	0.4	1.0 (Cons)	0.0 (Central)	LGL
B1	$\pi/4$	0.4	1.0 (Cons)	1.0 (Upwind)	LG
B2	$3\pi/4$	0.4	1.0 (Cons)	1.0 (Upwind)	LG
B3	$\pi/2$	0.4	1.0 (Cons)	1.0 (Upwind)	LG
C1	$\pi/4$	0.4	0.0 (Non-cons)	0.0 (Central)	LGL
C2	$3\pi/4$	0.4	0.0 (Non-cons)	0.0 (Central)	LGL
C3	$\pi/2$	0.4	0.0 (Non-cons)	0.0 (Central)	LGL

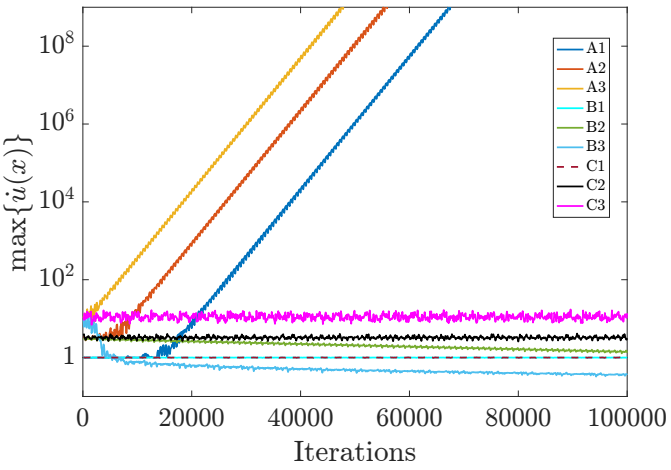

FIGURE 7. *Residuals of the numerical simulations performed for the three benchmark tests and computed by the three algorithms considered.*

travel with different speeds. However, the overall solution remained stable for large wavenumbers. This result can be also observed in the constant advection speed case, meaning it is inherent to the DG variant (i.e., Legendre-Gauss-Lobatto nodes).

5. Conclusions. We have presented an extension of the von Neumann stability analysis technique for non-constant advection speeds. The method has been used to study the dispersion and dissipation errors of various discontinuous Galerkin schemes. The new von Neumann analysis technique, when applied to the discontinuous Galerkin

method, enabled the analysis of the selection of nodal points, polynomial order, inter-element fluxes, and split forms. We have recovered well-known results from the classic constant advection cases and extended the results to non-constant advection speeds. We have shown that schemes that are stable when analysed with constant speed von Neumann analysis become unstable in the non-constant case (e.g. conservative DG with Legendre-Gauss-Lobatto points and central fluxes). The latter was already demonstrated experimentally in [6], but not theoretically analysed. Additionally, the non-conservative form provides a stable scheme for constant and non-constant advection speeds as long as the advection speed remains positive.

Appendix A. Detailed expressions of the von Neumann matrices.

Section 2 described the matrices of the complete system for multiple elements of the von Neumann analysis. These matrices are built as an element-wise combination of each DG system. For each element, its nodal degrees of freedom are governed by:

$$\frac{h}{2}\dot{\underline{\boldsymbol{Q}}}^{el} = \boldsymbol{L}^{el}\underline{\boldsymbol{Q}}^{el-1} + \boldsymbol{C}^{el}\underline{\boldsymbol{Q}}^{el} + \boldsymbol{R}^{el}\underline{\boldsymbol{Q}}^{el+1}, \tag{40}$$

where the matrices $\boldsymbol{L}^{el}$, $\boldsymbol{C}^{el}$, and $\boldsymbol{R}^{el}$ depend on the numerical fluxes, interpolation, integration nodes, and advection speed function. Their expressions are given in Eq. (21). When assembling the full mesh system, all nodal degrees of freedom are arranged in the array $\underline{\boldsymbol{Q}}$. The equations are then assembled in the new system, where two ghost cells for the boundary elements are included:

$$\frac{h}{2}\frac{d}{dt}\begin{Bmatrix} \underline{\boldsymbol{Q}}^1 \\ \underline{\boldsymbol{Q}}^2 \\ \underline{\boldsymbol{Q}}^3 \\ \vdots \\ \underline{\boldsymbol{Q}}^K \end{Bmatrix} = \begin{bmatrix} \boldsymbol{C}^1 & \boldsymbol{R}^1 & \boldsymbol{0} & \cdots & \boldsymbol{0} \\ \boldsymbol{L}^2 & \boldsymbol{C}^2 & \boldsymbol{R}^2 & \cdots & \boldsymbol{0} \\ \boldsymbol{0} & \boldsymbol{L}^3 & \boldsymbol{C}^3 & \cdots & \boldsymbol{0} \\ \vdots & \vdots & \vdots & \ddots & \vdots \\ \boldsymbol{0} & \boldsymbol{0} & \boldsymbol{0} & \vdots & \boldsymbol{C}^K \end{bmatrix} \begin{Bmatrix} \underline{\boldsymbol{Q}}^1 \\ \underline{\boldsymbol{Q}}^2 \\ \underline{\boldsymbol{Q}}^3 \\ \vdots \\ \underline{\boldsymbol{Q}}^K \end{Bmatrix} + \begin{Bmatrix} \boldsymbol{L}^1\underline{\boldsymbol{Q}}^0 \\ \boldsymbol{0} \\ \boldsymbol{0} \\ \vdots \\ \boldsymbol{R}^K\underline{\boldsymbol{Q}}^{K+1} \end{Bmatrix}. \tag{41}$$

The condensed version presented in Eq. (23) is:

$$\boldsymbol{C} = \begin{bmatrix} \boldsymbol{C}^1 & \boldsymbol{R}^1 & \boldsymbol{0} & \cdots & \boldsymbol{0} \\ \boldsymbol{L}^2 & \boldsymbol{C}^2 & \boldsymbol{R}^2 & \cdots & \boldsymbol{0} \\ \boldsymbol{0} & \boldsymbol{L}^3 & \boldsymbol{C}^3 & \cdots & \boldsymbol{0} \\ \vdots & \vdots & \vdots & \ddots & \vdots \\ \boldsymbol{0} & \boldsymbol{0} & \boldsymbol{0} & \vdots & \boldsymbol{C}^K \end{bmatrix}, \boldsymbol{L} = \begin{bmatrix} \boldsymbol{L}^1 \\ \boldsymbol{0} \\ \boldsymbol{0} \\ \vdots \\ \boldsymbol{0} \end{bmatrix}, \boldsymbol{R} = \begin{bmatrix} \boldsymbol{0} \\ \boldsymbol{0} \\ \boldsymbol{0} \\ \vdots \\ \boldsymbol{R}^K \end{bmatrix}. \tag{42}$$

Boundary conditions are applied for the ghost cells such that the matrix $\boldsymbol{M}(k)$ is built by combining $\boldsymbol{L}$, $\boldsymbol{C}$, and $\boldsymbol{R}$, as described in Eq. (27):

$$\frac{h}{2}\frac{d}{dt}\begin{Bmatrix} \underline{\boldsymbol{Q}}^1 \\ \underline{\boldsymbol{Q}}^2 \\ \underline{\boldsymbol{Q}}^3 \\ \vdots \\ \underline{\boldsymbol{Q}}^K \end{Bmatrix} = \begin{bmatrix} \boldsymbol{C}^1 & \boldsymbol{R}^1 & 0 & \cdots & \exp[-2ikT]\boldsymbol{L}^1 \\ \boldsymbol{L}^2 & \boldsymbol{C}^2 & \boldsymbol{R}^2 & \cdots & 0 \\ 0 & \boldsymbol{L}^3 & \boldsymbol{C}^3 & \cdots & 0 \\ \vdots & \vdots & \vdots & \ddots & \vdots \\ \exp[2ikT]\boldsymbol{R}^K & 0 & 0 & \cdots & \boldsymbol{C}^K \end{bmatrix} \begin{Bmatrix} \underline{\boldsymbol{Q}}^1 \\ \underline{\boldsymbol{Q}}^2 \\ \underline{\boldsymbol{Q}}^3 \\ \vdots \\ \underline{\boldsymbol{Q}}^K \end{Bmatrix}. \tag{43}$$

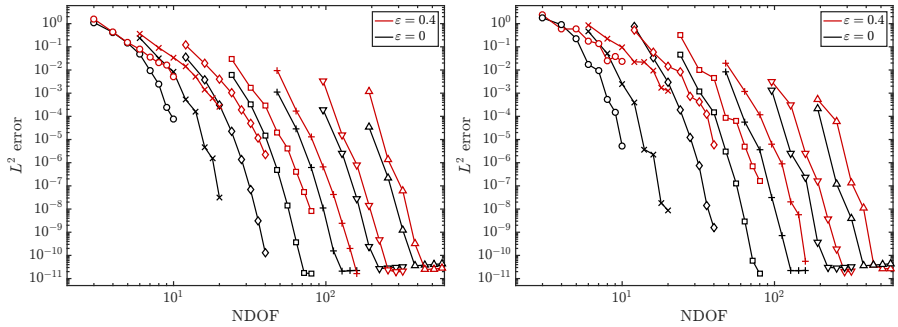

(a) DG with Gauss points and upwind fluxes. (b) Non-conservative DG with Gauss-Lobatto points and central fluxes.

FIGURE 8. *Convergence analysis of two stable DG configurations. The polynomial order N varies from 2 to 9 and the mesh sizes range from $h = 2$ ($K = 1$ elements) to 0.03125 ($K = 64$ elements). Each $h-$refined mesh results from the subdivision of the previous mesh. The number of degrees of freedom is defined as $NDOF = K(N+1)$. Black lines represent constant advection speed ($\varepsilon = 0$) and red lines represent non-constant advection with inhomogeneity $\varepsilon = 0.4$.*

Thus, a linear ordinary differential equation system with constant coefficients is obtained. The solution of the system is analysed by means of the eigenvalue problem described in section 2.

Appendix B. Convergence study on the numerical methods. To prove the consistency of the dispersion-dissipation analysis with the numerical solutions, we have performed a convergence analysis on the two DG configurations studied that provided a stable solution: DG with Gauss points and upwind fluxes, and non-conservative DG with Gauss-Lobatto and central fluxes. In this case, the solution of the non-constant advection speed is:

$$q_t + (1 + \varepsilon \cos \pi x) q_x = 0, \quad -1 \leq x \leq 1 \tag{44}$$

with $\varepsilon = 0.0$ (constant speed) and a fixed inhomogeneity of $\varepsilon = 0.4$. The initial condition is set to:

$$q_0 = \cos[\pi G(x) \bar{g}], \tag{45}$$

with a wavenumber $k = \pi$. We compute the L^2 error using the analytical solution:

$$q(x,t) = \cos[\pi G(x) \bar{g} - \omega t], \quad \omega = \pi / \bar{g} \tag{46}$$

and depict the convergence of hp-refinement in Figure 8. Although the classic DG (Gauss points with upwind flux) provides smoother convergence than the non-conservative scheme with central fluxes, similar accuracy and exponential convergence are observed for all cases. Additionally, we observed that the non-constant speed cases (inhomogeneity $\varepsilon = 0.4$) require finer discretisations to achieve similar accuracies to those achieved when considering constant advection speeds $\varepsilon = 0$.

REFERENCES

[1] M. Ainsworth, *Dispersive and dissipative behaviour of high order discontinuous Galerkin finite element methods* , Journal of Computational Physics, 198 (2004), pp. 106 – 130.
[2] F. Bassi and S. Rebay, *A high-order accurate discontinuous finite element method for the numerical solution of the compressible Navier-Stokes equations*, Journal of Computational Physics, 131 (1997), pp. 267 – 279.
[3] C. Canuto, M. Hussaini, A. Quarteroni, and T. Zang, *Spectral Methods: fundamentals in single domains*, Springer, 2006.
[4] C. Hirsch, *Numerical computation of internal and external flows: The fundamentals of computational fluid dynamics, 2nd Edition*, Butterworth-Heinemann, 2007.
[5] B. Cockburn, G. Kanschat, and D. Schötzau, *An equal-order DG method for the incompressible Navier–Stokes equations*, Journal of Scientific Computing, 40 (2009), pp. 188–210.
[6] D. A. Kopriva, and G. J. Gassner, *An energy stable discontinuous Galerkin spectral element discretization for variable coefficient advection problems*, SIAM Journal on Scientific Computing, 36 (2014), pp. A2076–A2099.
[7] D. A. Kopriva, A. R. Winters, M. Bohm and G. J. Gassner, *A provably stable discontinuous Galerkin spectral element approximation for moving hexahedral meshes*, Computers and Fluids, 000 (2016), pp. 1–13.
[8] D. N. Arnold, F. Brezzi, B. Cockburn and L. D. Marini, *Unified analysis of discontinuous Galerkin methods for elliptic problems*, SIAM J. Numer. Anal., 39 (5) (2001), pp. 1749–1779.
[9] E. Ferrer, *An interior penalty stabilised incompressible Discontinuous Galerkin - Fourier solver for implicit Large Eddy Simulations*, Journal of Computational Physics, 348 (2017), pp. 754–775.
[10] H. Elman, D. Silvester, and A. Wathen, *Finite elements and fast iterative solvers: with applications in incompressible fluid dynamics*, Oxford University Press, 2005.
[11] E. Toro, *Riemann solvers and numerical methods for fluid dynamics*, Springer, 2009.
[12] F. Bassy and S. Rebay, *High-order accurate discontinuous finite element solution of the 2D Euler equations*, Journal of Computational Physics, 138 (1997), pp. 251–285.
[13] E. Ferrer, D. Moxey, R. Willden, and S. Sherwin, *Stability of projection methods for incompressible flows using high order pressure-velocity pairs of same degree: Continuous and discontinuous galerkin formulations*, Communications in Computational Physics, 16 (2014), pp. 817–840.
[14] E. Ferrer and R. Willden, *A high order discontinuous Galerkin finite element solver for the incompressible Navier–Stokes equations*, Computers & Fluids, 46 (2011), pp. 224–230.
[15] E. Ferrer and R. H. Willden, *A high order discontinuous Galerkin - Fourier incompressible 3D Navier-Stokes solver with rotating sliding meshes*, Journal of Computational Physics, 231 (2012), pp. 7037–7056.
[16] F. Fraysse, C. Redondo, G. Rubio, and E. Valero, *Upwind methods for the Baer–Nunziato equations and higher-order reconstruction using artificial viscosity*, Journal of Computational Physics, 326 (2016), pp. 805 – 827.
[17] G. J. Gassner, *A kinetic energy preserving nodal discontinuous Galerkin spectral element method*, International Journal for Numerical Methods in Fluids, 00 (2013), pp. 1–27.
[18] G. J. Gassner, *An analysis of the dissipation and dispersion errors of the Pn-Pm schemes*, Journal of Scientific Computing, 54 (2013), pp. 21–44.
[19] G. J. Gassner, *A skew-symmetric discontinuous Galerkin spectral element discretization and its relation to SBP-SAT finite difference methods*, SIAM Journal on Scientific Computing, 35 (2013), pp. 1233–1256.
[20] G. D. Smith, *Numerical solution of partial differential equations, Finite difference methods* , Oxford Applied Mathematics and Computing Science Series, 1985.
[21] G. J. Gassner and A. D. Beck, *On the accuracy of high-order discretizations for underresolved turbulence simulations, A.D. Theor. Comput. Fluid Dyn. (2013) 27–221.*
[22] G. J. Gassner and D. A. Kopriva, *A comparison of the dispersion and dissipation errors of Gauss and Gauss-Lobatto discontinuous Galerkin spectral element methods*, SIAM Journal on Scientific Computing, 33 (2011), pp. 2560–2579.
[23] G. J. Gassner, A. R. Winters and D. A. Kopriva, *Split form nodal discontinuous Galerkin schemes with Summation-By-Parts property for the compressible Euler equations*, Journal of Computational Physics, in Press.
[24] G. Mengaldo, D. De Grazia, D. Moxey, P. E. Vincent and S. J. Sherwin , *De-aliasing techniques for high-order spectral element methods on regular and irregular grids*, Journal of Computational Physics, 299 (2015), pp. 56–81.
[25] D. Gottlieb and J. S. Hesthaven, *Spectral methods for hyperbolic problems*, Journal of Computational and Applied Mathematics, 128 (2001), pp. 83–131.

[26] D. Gottlieb and S. A. Orszag, *Numerical analysis of spectral methods: theory and applications*, SIAM, 1977.
[27] J. S. Hesthaven and T. Warburton, *Nodal discontinuous Galerkin methods: algorithms, analysis, and applications*, Springer Science & Business Media, 2008.
[28] H. Reed and T. R. Hill, *Triangular mesh methods for the neutron transport equation*, Technical Report LA-UR-73-479, Los Alamos Scientific Laboratory, (1973).
[29] J. Manzanero, G. Rubio, E. Ferrer, E. Valero, D.A. Kopriva, *Insights on aliasing driven instabilities for advection equations with application to Gauss-Lobatto discontinuous Galerkin methods*, Journal of Scientific Computing, (2017).
[30] G. E. Karniadakis and S. J. Sherwin, *Spectral/hp element methods for computational fluid dynamics*, Oxford Science Publications, 2005.
[31] M. Kompenhans, G. Rubio, E. Ferrer, and E. Valero, *Adaptation strategies for high order discontinuous galerkin methods based on tau-estimation*, Journal of Computational Physics, 306 (2016), pp. 216 – 236.
[32] M. Kompenhans, G. Rubio, E. Ferrer, and E. Valero, *Comparisons of p–adaptation strategies based on truncation– and discretisation–errors for high order discontinuous Galerkin methods*, Computers & Fluids, 139 (2016), pp. 36 – 46. 13th {USNCCM} International Symposium of High-Order Methods for Computational Fluid Dynamics - A special issue dedicated to the 60th birthday of Professor David Kopriva.
[33] D. A. Kopriva, *Implementing spectral methods for partial differential equations*, Springer Netherlands, 2009.
[34] R. Moura, S. Sherwin, and J. Peiró, *Eigensolution analysis of spectral/hp continuous galerkin approximations to advection–diffusion problems: Insights into spectral vanishing viscosity*, Journal of Computational Physics, 307 (2016), pp. 401–422.
[35] M. Owkes and O. Desjardins, *A discontinuous Galerkin conservative level set scheme for interface capturing in multiphase flows*, Journal of Computational Physics, 249 (2013), pp. 275 – 302.
[36] R. C. Moura, S. J. Sherwin and J. Peiro, *Linear dispersion-diffusion analysis and its application to under-resolved turbulence simulations using discontinuous Galerkin spectral/hp methods*, Journal of Computational Physics, 298 (2015), pp. 695–710.
[37] B. Riviere, *Discontinuous Galerkin methods for solving elliptic and parabolic equations: theory and implementation*, Society for Industrial and Applied Mathematics, Philadelphia, PA, USA, 2008.
[38] R. J. LeVeque, *Finite volume methods for hyperbolic problems*, Cambridge University Press, 2002.
[39] R. M. Kirby and G. Em Karniadakis, *De-aliasing on non-uniform grids: Algorithms and applications*, Journal of Computational Physics, 191 (2003), pp. 249–264.
[40] R. M. Kirby and S. J. Sherwin, *Stabilisation of spectral/hp element methods through spectral vanishing viscosity: Application to fluid mechanics modelling*, Computer Methods in Applied Mechanics and Engineering, 195 (2006), pp. 3128–3144.
[41] S. C. Spiegel, H. T. Huynh and J. R. DeBonis, *De-aliasing through over-integration applied to the flux reconstruction and discontinuous Galerkin methods*, 22nd AIAA Computational Fluid Dynamics Conference, AIAA Aviation, (AIAA 2015-2744).
[42] K. Shahbazi, P. Fischer, and C. Ethier, *A high-order discontinuous Galerkin method for the unsteady incompressible Navier–Stokes equations*, Journal of Computational Physics, 222 (2007), pp. 391 – 407.
[43] S. J. Sherwin, *Dispersion analysis of the continuous and discontinuous Galerkin formulations*, in in International Symposium on Discontinuous Galerkin Methods, Springer, 1999, pp. 425–431.
[44] T. C. Fisher and M. H. Carpenter, *High-order entropy stable finite difference schemes for nonlinear conservation laws: Finite domains*, Journal of Computational Physics, 252 (2013), pp. 518–557.
[45] H. Versteeg and W. Malalasekera, *An Introduction to computational fluid dynamics, the finite volume method*, Pearson, 1996.
[46] P. Vincent, P. Castonguay, and A. Jameson, *Insights from von Neumann analysis of high–order flux reconstruction schemes*, Journal of Computational Physics, 230 (2011), pp. 8134 – 8154.
[47] V. S. Ryaben'kii and S. V. Tsynkov, *A theoretical introduction to numerical analysis*, CRC Press, 2006.
[48] J. Watkins, K. Asthana, and A. Jameson, *A numerical analysis of the nodal discontinuous Galerkin scheme via flux reconstruction for the advection-diffusion equation*, Computers & Fluids, (2016).

[49] J. Williamson, *Low-storage Runge-Kutta schemes*, Journal of Computational Physics.
[50] O. Zienkiewicz and K. Morgan, *Finite elements and approximation*, John Wiley & Sons Inc, 1983.